Evaluation of UAV Configurations for Package Delivery Missions though Conceptual Design

Bharath Govindarajan[1] **and Ananth Sridharan**[2]

[1]Assistant Professor, Dept. of Aerospace Engineering, Indian Institute of Technology, Madras, India
[2]Aircraft Design Engineer, A^3 by Airbus, Sunnyvale, CA, USA

ABSTRACT

Conceptual sizing and performance estimation of four configurations for a package delivery mission is presented in this work. The multi-fidelity VTOL design framework HYDRA is used to size a notional quadcopter, hexacopter, quad-rotor bi-plane tailsitter (QBiT), and a lift-augmented tricopter for weight classes of 10 kg, 15 kg, 20 kg, and 25 kg. Sizing is performed using a combination of physics-based empty weight models for the airframe, rotor blades and wings, along with empirical models. A longitudinal trim methodology was implemented that minimizes the power required for a configuration for a given flight condition. Representative payload drop scenarios were constructed from different cruise speeds and ranges to identity a vehicle design in each configuration that can complete the most number of payload drop missions successfully. It is identified that the hexacopter performed better over the quadcopter in terms of requiring lower installed power and deliver heavier payload packages for a given radius of action. Wing-based designs such as the QBiT and tricopter are capable of delivering packages in a short time owing to either full/partial conversion to airplane mode during cruise flight.

INTRODUCTION

With the introduction of expedited package delivery services, an increasing number of customers may come to rely on rapid delivery for their purchases. Package delivery within a few hours from the placement of the order may be enabled by Unmanned Aerial Vehicles (UAVs). Design of this UAV platform requires knowledge of the rate of packages requested in the area, as well as the size and weight of these packages. For a given urban region, the system level design also includes the location of a central and forward warehouses, possible requirements of ground supply units, and a communication system to handle the vehicles in the air.

There are a few organizations that have already taken to the skies in their effort to deliver small-scale supplies via air; some concepts are shown in Fig. . Matternet with UPS (Ref. 1) have planned to deliver collected blood samples to hospital in North Carolina. Zipline (Ref. 2) are flying medical supplies to remote location in Rwanda, and Swoop Aero (Ref. 3) has been delivering vaccines to remote islands in the pacific. There is also a larger category of UAVs capable of carrying mugh larger payloads, and these vehicles are classified as cargo drones. Sabrewings' "Rhaegal" (Ref. 4) is being designed to fly at 180 knots at a cruise altitude of 22,000 ft. Nautilus has designed a 30 ft prototype that can deliver 700 lbs at a distance of 2,500 nautical miles. They also plan to design a 2 ton vehicle the size of a Boeing-777 (Ref. 5). While these cargo drones can to fly further and carry more payload compared to small scale drones, the focus of this paper is limited to drones that deliver packages in and around urban settings.

Next-generation UAVs capable of coordinating with each other in congested airspace are envisioned with new vehicle concepts that are: (1) Compact, (2) Efficient in both hover and cruise, (3) Quiet (reduced acoustic signature), (4) Agile (maneuverable in tight spaces) and (5) Gust-tolerant. Alongside the civilian space, these platforms can transform and expand the capability in military operations as well in a wide range of environments. Figure shows a few unmanned VTOL configurations developed by various entities for delivery of packages, medical supplies for use in the urban environment and remote locations. Each of these designs are vastly different from the conventional single main rotor, coaxial, tandem, or tiltrotor/tilt-wing configurations. They feature some form of thrust and/or lift augmentation, distributed propulsion, and embedded rotors. A common feature in several such designs is the ability to perform vertical take-off and landing (VTOL). Each configuration may also feature varying levels of compromise between hover and cruise efficiencies over the mission profile. Table 1 shows available details on some of these configurations. These designs feature a distinct separation of hover thrust and cruise propulsion using fixed-tilt rotors in various orientations ("lift" rotors and "cruise" propellers). The *Wingcopter* concept, however, uses tiltable prop-rotors to power both hover and cruise flight, which is aerodynamically advantageous as the rotors operating only in axial flight.

Submitted to the European Rotorcraft Forum, 2019

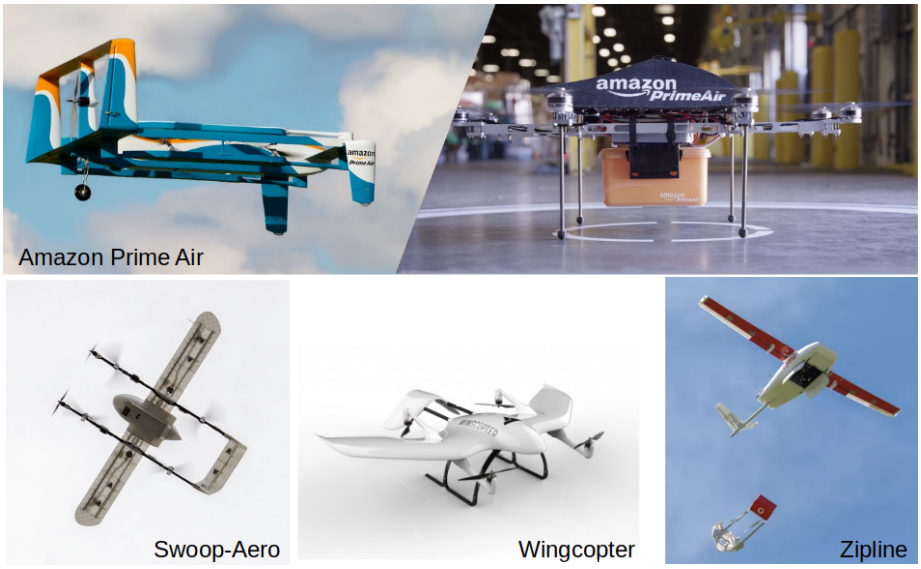

Fig. 1. Some unmanned drones concepts used for commercial package delivery and/or medical aid.

The design and sizing procedures, empty weight models, and performance characteristics for these configurations are typically not available in public literature and encapsulate several unstated and often proprietary assumptions/criteria across a range of operating conditions. Additionally, owing to the vast variety in unique layouts of rotors and wings, the sizing laws and performance/drag/controllability trade-offs are configuration-specific and cannot be transplanted directly to other very different configurations. It is not immediately apparent upon inspection if there is a preferred configuration that is most suitable for a given mission and payload. For some combinations of mission profile and geometric scale, tilting prop-rotors may prove advantageous overall, while the "lift+cruise" configurations may prove more useful for other missions.

Table 1. Available weight and performance metrics of some UAV drones

Concept	Configuration	Payload/Range/Endurance
Prime Air 1 Prime Air 2 Prime Air 3	Quadrotor Lift + cruise Octorotor	5 lb, 10 miles, 30 min
Swoop aero	Lift+cruise 2 tractor props	2.5 kg, 1 hr endurance 110 kmph V_{max}
Wingcopter	Quad tilt-rotor Blown wings	6 kg for 45 km V_{cruise} = 150 kmph

Requirements in Urban Settings: Background

The American Helicopter Society in their 32nd annual student design competition (Ref. 6) requested proposals for a package delivery scenario in an urben environement that warranted a system-of-systems design. Understanding the requirements of the servicing-region is essential in determining the required characteristics of UAV, such as it payload capacity, maximum range, cruise speed, and hovering parameters. The design report from the University of Maryland (Ref. 6) details the results of a package delivery simulation to determine the sizing mission. In this simulation, 5,000 packages are ordered within a 10 hour window over a 50-mile $\times$ 50-mile area of varying payloads. Up to 85% of the packages were of 5 lbs or lesser in weight. Conditions stipulated that the packages must reach the destination within 2 hours of placing the order. Multiple trade studies were conducted and the effect of number of forward supply locations, presence of charging stations, ability to deliver multiple packages, and multiple vehicle designs were assessed. An adaptation of the traveling salesman algorithm was used to analyze these results (Ref. 6). It was determined that 480 aerial vehicles were required to service such a request. This number was a sum total of the vehicles currently out on delivery, those being currently loaded with packages, and with a buffer for vehicles that might require servicing/maintanence down-time. The optimal solution also required the vehicles to deliver multiple packages on a single trip from and to the central warehouse. No forward supply stations or additional ground vehicle support was deemed necessary. The path planning of a fleet of vehicles is an exercise in itself, and is beyond the scope of the current work. Lessons learned from past studies are used to design the sizing mission that is used in the present work.

Objectives

The primary objectives of this paper are to

1. Perform sizing for different UAV configurations for various mission profiles
2. Optimize each configuration for a given mission and evaluate performance in off-sizing conditions

3. Identify best-suited designs for various types of missions (combinations of range, cruise speed and payload)

METHODOLOGY

To assess with confidence the relative merits of one configuration over others, a robust and flexible sizing tool is required that enables the designer to capture the various physical phenomena that manifest in VTOL platform featuring multiple rotors, wings and electric motors. The sizing analysis HYDRA (HYbrid Design and Rotorcraft Analysis) has been developed by the authors since 2015, and previously used to analyze both conventional and unconventional helicopters, compound rotorcraft and unconventional VTOL platforms at full-scale, intermediate-scale and sub-scale. (Refs. 7–9). HYDRA also incorporates—within the sizing loop—physics based models to capture the weight of certain sub-components and comprehensive analysis to predict the power requirements under different flight conditions (Ref. 10).

A vehicle configuration is defined within HYDRA as a collection of basic components such as rotors, wings, and fuselage with their orientations and location defined relative to the vehicle body axes. Wing lift and drag variations with angle of attack are incorporated through look-up tables for the airfoil section, with 3-d corrections in the linear lifting range of angle of attack.

Because these unconventional aircraft with redundant flight controls may feature multiple trim solutions (depending on the flight condition), trim is performed through an optimization process, which targets the minimization of total aerodynamic power required subject to equality constraints defining the trim condition (zero acceleration). The trim variables are rotor thrusts and fuselage attitude, for longitudinal (non-turning) flight. This approach was previously presented for fixed-wing aircraft (Ref. 11), and the general technique was recently adapted to a vertical-lift tandem tilt-wing configuration with redundant actuators (Ref. 12).

Trim Process

The power required during a mission segment is coupled to the trim process, where the longitudinal forces are in balance such that the net acceleration is zero. The trim equations are set up in the body axes. Forces resolved along the body-axes are:

1. Weight
2. Wing lift and drag
3. Fuselage drag
4. Rotor thrust(s)

The formulation assumes that the wing and the rotor can be tilted, so as to model a tilt-rotor or a tilt-wing configuration. The wing rotation angle is denoted by θ_W, which is the trim variable representing the tilt of the wing reference root chordline relative to the fuselage mount setting. The rotor tilt angle (for a tilt-rotor) is represented by θ_R, which denotes the longitudinal tilt angle of the rotor shaft relative to its mount on a fixed wing or fuselage. These angles are schematically shown in Fig. 2(a). For the quad-rotor bi-plane configuration shown in Fig. 2(b), θ_W and θ_R are set to zero. For a tilt-wing configuration with the rotor fixed to the wing, θ_R is set to zero, and for a tiltrotor configuration, θ_W is set to zero. The equations along the x and z body axes are given by

$$\begin{aligned} F_x &= \sum_{i=1}^{N_R} T_i \cos(\theta_W + \theta_R) - W \sin\theta_F - D_F \cos(\theta_F - \gamma) \\ &+ \sum_{i=1}^{N_W} L_i \sin(\theta_F - \gamma) - \sum_{i=1}^{N_W} D_i \cos(\theta_F - \gamma) \qquad (1) \\ F_z &= -\sum_{i=1}^{N_W} L_i \cos(\theta_F - \gamma) + W \cos\theta_F - D_F \sin(\theta_F - \gamma) \\ &- \sum_{i=1}^{N_W} D_i \sin(\theta_F - \gamma) - \sum_{i=1}^{N_R} T_i \sin(\theta_W + \theta_R) \qquad (2) \end{aligned}$$

where W is GTOW, D_F is the fuselage drag, T_i is the thrust of the i^{th} rotor, L_i is the lift of the i^{th} wing, and D_i is the drag of the i^{th} wing. The trim vector is given by

$$\begin{aligned} X &= [T_1, T_2, ..., T_{N_R}, (\theta_W)_1, (\theta_W)_2, ..., (\theta_W)_{N_W}, \\ &\quad (\theta_R)_1, (\theta_R)_2, ..., (\theta_R)_{N_R}, \theta_F]^T \qquad (3) \end{aligned}$$

The lift on the wing is not a trim variable and is computed based on the dynamic pressure, and the angle of attack given by $(\theta_W + \theta_F) - \gamma$. A generic high-lift angle of attack table (as shown in Fig. 4) is part of the HYDRA library, which is used to compute the lift, and drag on the wing.

For a configuration like the quad-rotor bi-plane tailsitter or a propeller-wing combination, the effect of the propwash on the wing is an important effect that must be taken into account. Figure 3 shows the vectorial respresentation of the change in effective angle of attack of the freestream vector in the presence of downwash. Note that the diagram is rotated so as to depict the freestream vector as horizontal to the page. The rotor wake is assumed to be completely contracted in accordance with momentum theory, i.e., $A_{\text{wake}} = 0.5 A_{\text{rotor}}$ and the downwash velocity is given by $V_d = 2\sqrt{T/(2\rho A)}$. For sections of the wing under the influence of the propwash, the reduction in angle of attack, ϕ, is given by

$$\phi = \tan^{-1}\left[\frac{V_d \sin(\theta_f - \gamma)}{V_\infty + V_d \cos(\theta_f - \gamma)}\right] \qquad (4)$$

and the net velocity magnitude is given by

$$V_\infty(\text{propwash}) = \sqrt{[V_d \sin(\theta_f - \gamma)]^2 + [V_\infty + V_d \cos(\theta_f - \gamma)]^2} \qquad (5)$$

Fuselage drag in pure hover (vertical) is accounted via the download factor, and via the equivalent flat-plate area in pure cruise (horizontal). For transition flight conditions, the fuselage is modelled as a cylindrical body and the model for drag estimation is presented in a subsequent section.

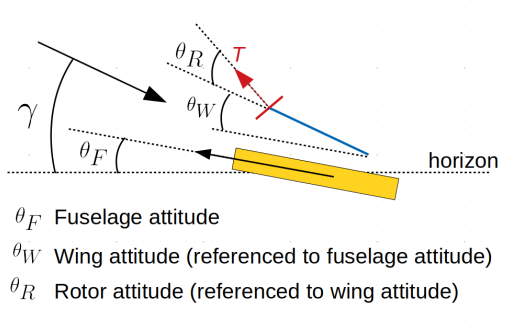

(a) Angles

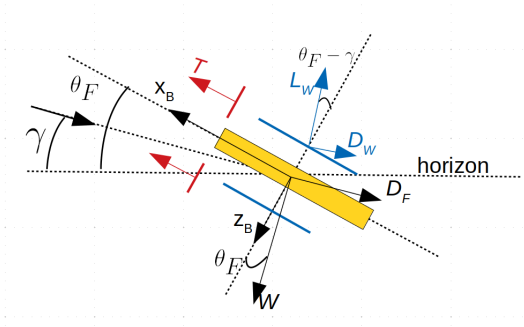

(b) Quad-rotor bi-plane example

Fig. 2. Schematic of trim angles and an example of the longitudinal forces on a quad-rotor bi-plane configuration.

Trim is set up as an optimization process with the objcetive function being the minimization of power consumed, subject to the constraints of $F_x = F_Z = 0$, as specified in Eqs. 1 and 2, i.e., zero acceleration in the longitudinal mode. Bounds are set on the trim variables so that $T_i \in [0, \infty)$ and $\{\theta_R, \theta_W, \theta_F\} \in [-\pi, \pi]$. Currently the Sequential Least Squares Programming (SLSQP) routine in Python's SciPy library ((Ref. 13)) is used to perform the optimization.

For a given thrust T, the power consumed by the rotor is obtained through modified momentum theory, whose salient equations are outlined here. From basic momentum theory in forward flight, the solution for the required power is given by

$$P = \kappa T(V_\infty \sin\alpha + V_i) + P_0 \tag{6}$$

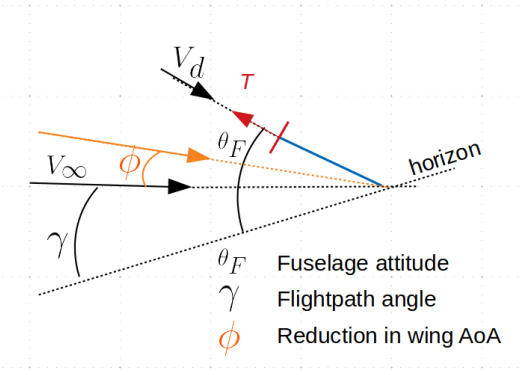

Fig. 3. Modification of the angle of attack and the velocity vector in the presence of propwash.

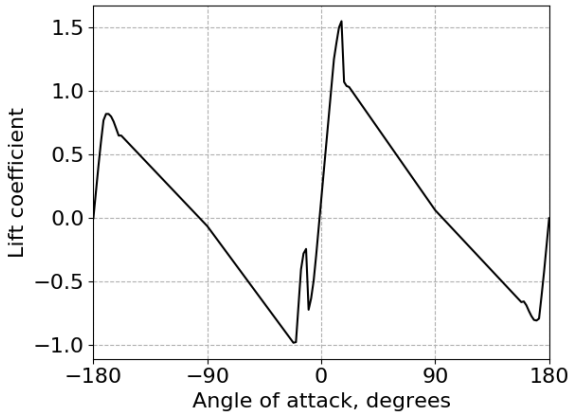

(a) Lift

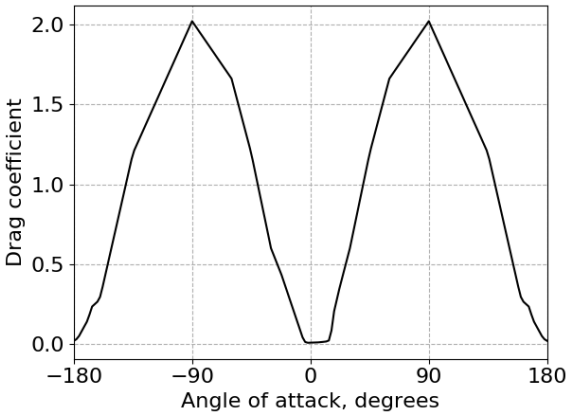

(b) Drag

Fig. 4. High angle lift and drag table used to obtain the forces on a wing during the sizing process.

where V_∞ is the forward flight speed, V_i is the induced velocity, α is the shaft-tilt angle, and P_0 is the profile power computed by

$$P_0 = \frac{\sigma c_{d_0}}{8}(1 + 4.65\mu^2)(\rho A(\Omega R)^2) \tag{7}$$

where c_{d_0} is the zero-lift drag of the airfoil, set to 0.012. The inflow equation for $\lambda = (V_\infty \sin\alpha + V_i)/(\Omega R)$ is given by

$$\lambda = \mu \tan\alpha + \frac{C_T}{2\sqrt{\mu^2 + \lambda^2}} \tag{8}$$

where $\mu = V_\infty \cos\alpha/(\Omega R)$ is the advance ratio, and $C_T = T/(\rho A(\Omega R)^2))$ is the non-dimensional thrust coefficient. For any flight condition, the resultant shaft tilt angle $(\theta_F - \gamma)$ can be thought of as the effective angle of attack of the rotor plane relative to the free-stream flow (positive when rotor disk is tilted down with its upper surface facing the free-stream flow). Rotor shaft power in edgewise forward flight can be obtained using an iterative solver for the inflow equation. At the extreme condition of $\alpha = \pi/2$, the forward flight equations fall onto the equation for vertical climb (i.e. axial flight). Thus, the presented unified formulation is used to obtain the power

in hover, edgewise forward flight, vertical climb as well as transition flight modes.

Empty weight models

Rotor weight model For small-scale VTOL with very stiff rotor systems, extrapolation of the blade weight trend lines (developed for full-scale helicopters) beyond the range of available data yields erroneous estimates for rotor blade weight (Ref. 9). An alternate approach using a physics-based estimation of weight was developed by the authors, and used in this work to estimate blade mass.

A schematic of the blade spar and cross-section parameters is shown in Fig. 5(c). The cross-section of the airfoil consists of a trapezoidal spar, skin, honeycomb material and a leading edge weight (to place the cross-section CG at quarter-chord). For each of these four components, materials are assigned from a database consisting of mass density, Young's modulus and allowable stress/strain in compression and tension. With rotor radius R, rotor speed Ω and peak torque at the blade root Q_b obtained from sizing, the vertical force on the blade and the corresponding bending moments are estimated with an assumed spanwise load distribution, with appropriate load factors and safety margins. Blade pre-cone for a stiff rotor design is used to reduce the axial stress resulting from the distributed lift. The shear load, centrifugal load loads and lift bending moments are used to size the blade cross-section and estimate mass of the blade. The skin is sized to ensure that the first torsion frequency is above 3/rev. A NACA-0012 section is used to estimate cross-section areas, moments of inertia and moments of area for the filler material (rohacell), skin (+/-45 deg carbon fiber sheet) and spar (0/90 carbon fiber webs, uniaxial carbon fiber caps).

Airframe weight model Parametric power law type models for estimating airframe weights, originally developed for single main rotor helicopters, feature the same limitations as those developed for rotor blades: at smaller scales, these models may provide erroneous weight estimates when used for airframes with significantly different load paths. In the present work, another physics-based approach for weight estimation is used: the airframe is defined as a beam lattice framework and the loads on the structure are computed using a static finite element analysis (FEA). An example of the finite element framework is shown in Fig. 5(b) for the QBiT design. The external loads on the structure arise from the weight of different components and the dominant aerodynamics loads (rotor thrust, torque and wing lift, drag). A set of three-dimensional Euler-Bernoulli beam finite elements with six degrees of freedom at each node (three translations and three rotations) are assembled and sized in an inner-loop within sizing.

The external loads corresponding to each mission phase are applied on the structure, and the resulting stresses and deflections are calculated and stored at all the nodes. Subsequently, the cross-section dimensions of the beams are iteratively resized to ensure; (i) Minimum factor of safety of 1.5 (based on Von-Mises stress) at a load factor of 3.5, (ii) A maximum deflection of 10% for any node (relative to its distance from the vehicle center). The cross-sections of all beam elements are assumed to be hollow circles with wall thickness equal to 15% outer radius. The only design parameter for a beam element is the outer radius of the cross-section. Beam cross-section radii for all elements are updated iteratively until the 3 design criteria are satisfied, and the weight of the airframe members is calculated using material density and final dimensions. The finite element analysis iterations are performed within the sizing loop and adds to the computational cost. The airframe weight is computed by multiplying the total volume of all the beam elements with the material density (for Aluminum, 2,700 kg/m^3). This weight is used to compute the vehicle empty weight component for the airframe structural members.

Drivesystem In the present work, the weight of all configurations considered were less than or equal to 25 kg GTOW. A preliminary study was performed to compare two drivetrain configurations: 1. An all-electric power supply using Lithium-Ion batteries, or 2. A hybrid piston engine electric combination with the piston engine running a generator, which then powers the motors and finally the rotors. In a previous study conducted by the authors (Ref. 7), the smallest available piston engine was Lycoming EL-005 with a dry weight of 6.35 kg (14 lb) and a maximum mechanical power output of 2.98 kW (4 hp), which was the engine frozen for this study. However, the drivetrain weight of piston engine along with the generator, combined with the losses in transmission efficiency dictated that a pure electric Lithium-Ion battery option was preferred and is the only powerplant option utilized in this study across all configurations.

The weights of batteries and electric motors are very well represented using statistical models. In the current study, the all-electric powerplant is modeled as a series of Lithium-polymer batteries, electric motors and electronic speed controllers. Figures 5(d) and 5(e) show the trendlines in battery specific energy and electric motor power-to-weight ratio, respectively, for commercially available designs where each data point represents a manufactured unit. Arguably, a battery density of 158 W-hr/kg is quite low and improvements can be made; this "conservative" design is typical of commercially available battery packs including the safety casing. Though electric motor weights are strictly driven by peak torque requirements, the data correlation between weight and peak power is also very good, primarily because most small Brushless DC (BLDC) motors operate at similar ranges of RPM. The electronic speed controller is sized based on the current drawn by the system assuming a 12 Volt source for the 20-lb and 50-lb vehicles. The variation of motor and speed controller weights with the peak motor power rating P (hp) is

$$
\begin{aligned}
W_{\text{motor}}(lb) &= 0.412\ \text{P} && \text{P} \leq\ 13.4\ \text{hp} \\
W_{\text{ESC}}(lb) &= 0.591\ \text{P} && \text{P} \leq 13.4\ \text{hp} \\
W_{\text{motor}} + W_{\text{ESC}}(lb) &= 1.489\ \text{P}^{0.783} && 13.4\ \text{hp} < \text{P} \leq 350\ \text{hp}
\end{aligned}
$$

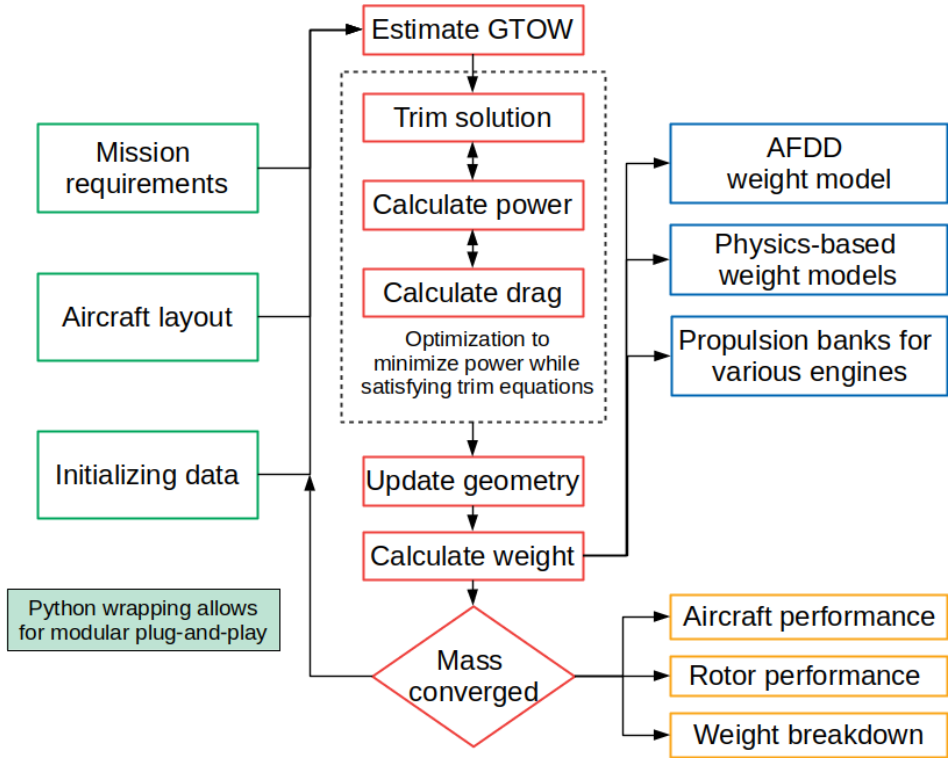

(a) Iterative sizing methodology

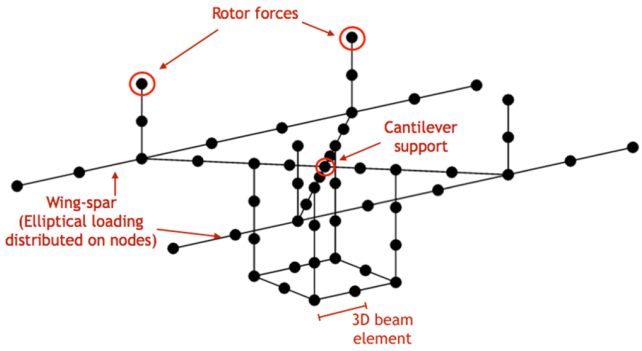

(b) Airframe weight model

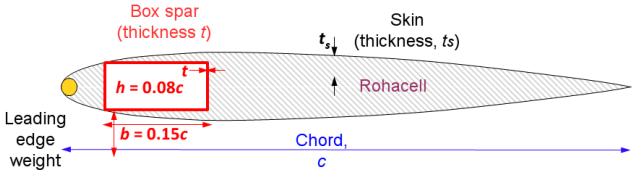

(c) Rotor blade weight model

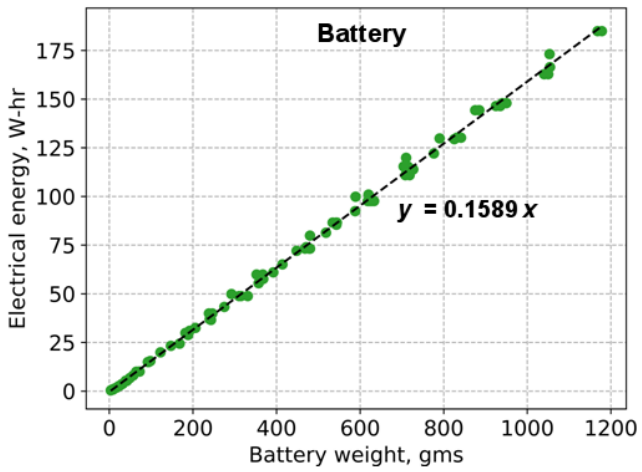

(d) Battery weight model

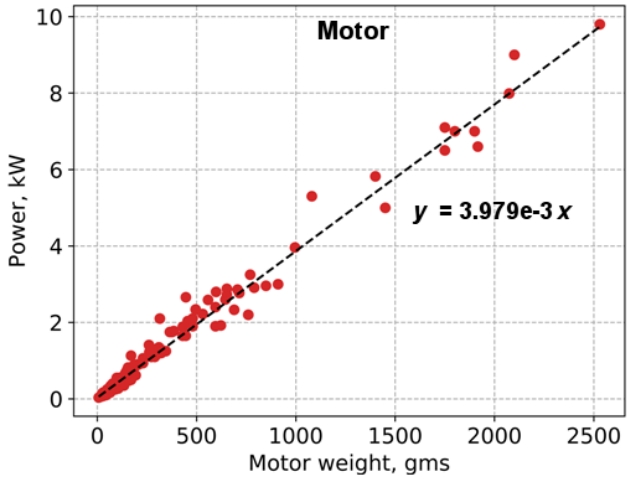

(e) Motor weight model below 10kW

Fig. 5. Preliminary sizing methodology and empty weight models for airframe, rotor blades, Lithium-polymer battery and D.C. brushless motors at sub-10kW rating.

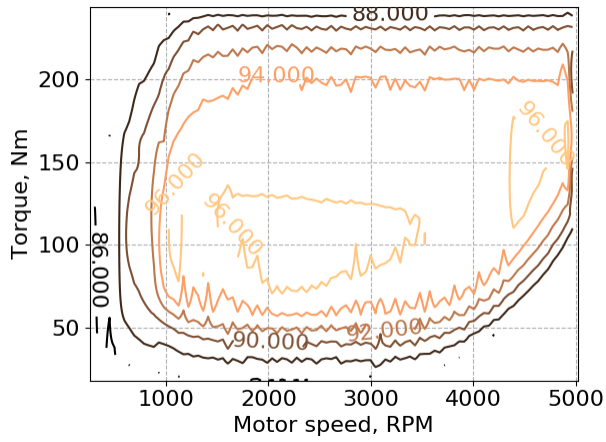

Fig. 6. Motor efficiency curves of the EMRAX228 used in the present study.

For sizing the motor, an overload factor of 2.0 (i.e., 100% excess power margin) is included to ensure that transients and gusts do not result in an uncontrollable flight conditions. Figure shows the motor efficiency as a function of the torque required and RPM, which in the drivetrain design, is the propeller RPM. The efficiency charts were obtained from the EMRAX228 motor specifications. The efficiency varies between 88% – 96% based on the operating state of the propeller.

Wing weight model For vehicles with fixed wings, the sizing is performed assuming minimum gauge for the skin (two layer of bi-directional carbon fiber) and filler material, with no leading edge weights. Owing to the smaller geometric scales, structural dynamics/resonance concerns may be ignored at this stage of the design. The skin is assumed to carry both torsion moment and bending moment. Shear is carried by a web within the airfoil section, consisting of two layers of bi-directional carbon fiber.

Miscellaneous weight For payload handling/drop and repositioning inside the cargo bay, an extra 1 lb of actuator and actuator battery mass is allocated. Additionally, the weights of wires, fasteners, nuts, bolts and other adhesives is accounted for through a weight margin equal to 10% of the vehicle empty mass. A recovery parachute (for safety) is also included, with mass modeled as 5% of take-off mass. This 15% of total weight was arrived at by studying the design of the 20 lb QBiT design (Ref. 14).

Aerodynamic models

Rotor performance: Rotor performance is estimated using modified momentum theory. While HYDRA has the capability of including Blade Element Momentum Theory (BEMT) directly into the sizing loop, certain configurations in the study operate their rotors in edgewise flight where BEMT is not applicable. For a configuration such as the QBiT where the rotors operate most of the time in propeller mode, BEMT could be used to provide valuable insight into the design of the rotor blade. However, to preserve parity in the fidelity of models across configurations, a modified momentum theory was used.

Based on experimental studies conducted by Winslow et al. (Ref. 15) on rotor blades for micro air vehicle configurations, the best figure of merit (FM) attainable was 0.66 for a rotor in hover supporting a vehicle with mass less than 100 grams. In the present study, a rotor figure of merit of 0.65 was assumed, which also includes interference effects of the rotor with the airframe. Forward flight power was computed based on the induced power factor and the profile drag of the rotor given by Eqs. 6–8, with the induced power factor (κ) calculated by equating the expressions in hover

$$\begin{aligned} \frac{1}{FM}\frac{T^{3/2}}{\sqrt{2\rho A}} &= \kappa\frac{T^{3/2}}{\sqrt{2\rho A}} + P_0 \\ \kappa &= \frac{1}{FM} - \frac{\sqrt{2\rho A}}{T^{3/2}}P_0 \\ \kappa &= \min(\kappa, 1.15) \end{aligned} \tag{9}$$

Here, P_0 is given by Eq. 7. A minimum value of 1.15 is imposed on the induced power factor to prevent values that are impractical.

Wing performance: Wing performance is not directly estimated, but the forces generated by the wing are included in the trim solution, which in turn predicts the thrust required by the rotor for a given flight condition. The lift and drag of the wing is based of a notional airfoil whose characteristics are shown in Figs. 4(a) and 4(b), respectively. The induced drag produced by the wing is based on the aspect ratio of the wing (AR) and the Oswalds efficiency factor (e, set to 0.8) given by

$$D_{\text{induced}} = \frac{C_L^2}{\pi\ \text{AR}\ e} q_W S_W \tag{10}$$

where C_L is the wing lift coeffient, q_W is the dynamic pressure of the wing, and S_W is the wing area. If the portion of the wing is under the influence of prop-wash, then the dynamic pressure is adjusted accordingly.

Fuselage drag estimation: The centerbody of the airframe (where the package is housed) is assumed to be a cylindrical cargo compartment with a hemispherical fairing on top. Hoener (Ref. 16) presents an expression for the variation of drag of a circular cylinder at various angles to the flow (Chapter 3, Figure 18). The drag coeffient of the fuselage is adapted as

$$C_D = 0.1 + 0.2\sin^3\alpha \tag{11}$$

where α is the angle of the attack between the axis of the cylinder and the freestream vector. Note that the drag coeffient of the vehicle when aligned to the flow is one-third of the value when exposed to it sideways. This variation is important when discussing the cruise speeds of configurations that fly edgewise versus those that "tilt" into the flow. The

reference area is the cylinder radius times the length of the cylinder. The fuselage radius and length are estimated in a similar approach used in Ref. 9, which was based on the design of the QBiT (Ref. 14).

Sizing for a Fixed Take-off Weight

The sizing methodology usually requires specification of a fixed payload, and allows the gross weight to converge using fixed-point iterations starting from an initial guess. However, depending on the combination of disk loading, tip speed, rotor solidity, mission parameters, and payload, the sizing iterations may diverge due to the classical weight ballooning problem. This numerical divergence may be a result of the relaxation factors used in the fixed point iterations, or may be an infeasible combination of sizing parameters.

Instead, it may be advantageous to identify the payload for a given mission with a fixed take-off weight (usually imposed through operational regulations). Therefore, the sizing process was modified to hold the take-off weight fixed, and calculate the payload that can be carried for a given mission. In this method, several weight groups in the vehicle remain fixed (e.g. airframe, powerplant, rotor blades and wings). The only variable during sizing iterations is the payload weight. In this manner, weight ballooning is avoided, and infeasible designs are identified as those combinations of parameters which result in zero or negative payload.

RESULTS

Validation

The basic sizing framework of HYDRA has been validated against the industry standard formulation (NDARC) (Ref. 17) for large scale configurations for which traditional empty weight models are application. Another validation effort was carried out for this paper where a single main rotor configuration was compared between the two code-suites. The chosen mission consists of a hover, cruise, and a loiter segment with the details presented in Table 2. The number of blades, rotor radius, tip speed, and blade aspect ratio were sizing inputs to both formulations. In HYDRA, the AFDD weights were used to assess the empty weight, and the calculation of rotor power and drivetrain equations are as outlined in the methodology section.

Table 2. Mission profile for comparison

Segment	Time	Airspeed	Altitude
Hover	5 min	0 knots	4,000 ft
Cruise	1.5 hours	157 knots	6,000 nm
Loiter	5 min	70 knots	0 ft

Figure 7(a) shows a comparison of the predicted empty weight, fuel weight, payload, and gross take-off weight between NDARC and HYDRA. Overall, good agreement was

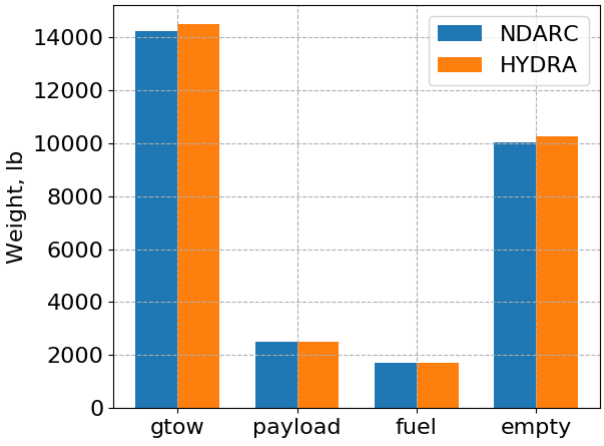

(a) Weight comparison

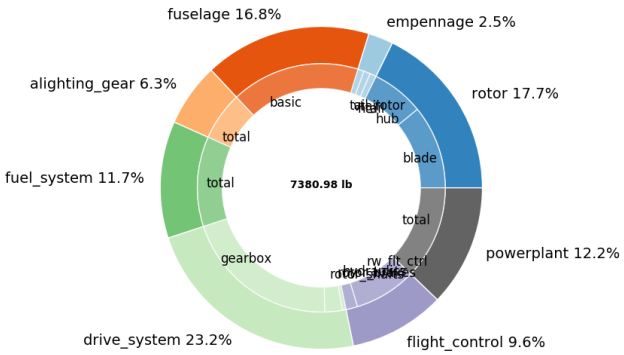

(b) Empty weight breakdown

Fig. 7. Comparison of gross weight parameters between HYDRA and NDARC along with the empty weight breakdown of the vehicle from HYDRA.

obtained between the two formulations. The maximum error across weight categories is less than 0.75%. A further breakdown of the empty weight is shown in Fig. 7(b). The different components are shown in the outer circle along with their percentage contribution to the empty weight. The breakdown of weight categories into subcomponents are shown in the inner circle. HYDRA was used to design a quad-rotor bi-plane tailsitter with a gross weight of 20 lb (9.1 kg) using physics based weight and performance models. A picture of the constructed prototype is shown in Fig. 8 and is currently undergoing flight testing.

Inclusion of Propwash over Wings

To assess the influence of propwash on the wing on the final design of a vehicle, a quad-rotor bi-plane tailsitter (QBiT) configuration (example shown in Fig. 8) was sized with and without the influence of the propwash on the wings. Equations 4 and 5 show that the presence of proprotors in the proximity of the wing will:

1. Increase the dynamic pressure over sections of the wing

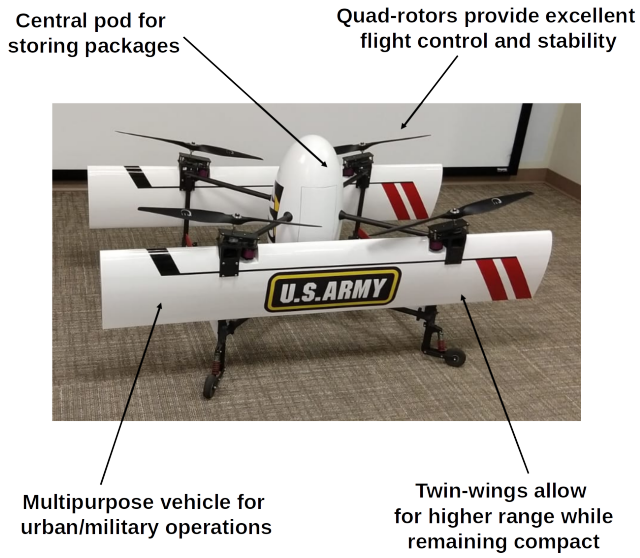

Fig. 8. 20 lb quad-rotor bi-plane tailsitter concept designed using HYDRA.

Table 3. Mission profile and gross parameters for assessing influence of propwash on vehicle sizing

Segment	Time	Airspeed
Hover	2 min	0 knots
Cruise	30 min	35 knots
Hover	5 min	0 knots
Cruise	30 min	35 knots
Parameter	**Without interference**	**With interference**
Payload	1.79 kg (3.94 lb)	1.81 kg (3.99 lb)
Empty weight	7.28 kg (16.06 lb)	7.26 kg (6.01 lb)

under the propwash, and

2. Reduce the angle of attack of the wing.

A notional sizing mission was chosen consisting of two hover and two cruise segments at MSL ISA conditions, as outlined in Table 3. The vehicle was sized to a fixed take-off mass of 9.1 kg (20 lb) and the propulsion system was based on batteries and DC motors.

Figure 9(a) shows the total power required in level forward flight for the sized QBiT as a function of cruise airspeed, with and without the effect of the propwash interference on the wing. At each flight speed, the vehicle was trimmed to enforce longitudinal force balance with zero accelerations while minimizing total shaft power. For the case where the interference effect is included, the required power is maximum at hover, decreases to a minimum at a certain forward flight speed and increases again at high cruise speeds, simiilar to a conventional helicopter.

When the effect of rotor wake on the wing operating angle of attack is excluded, the power required in transition is primarily driven by wing drag during stalled flight. As the

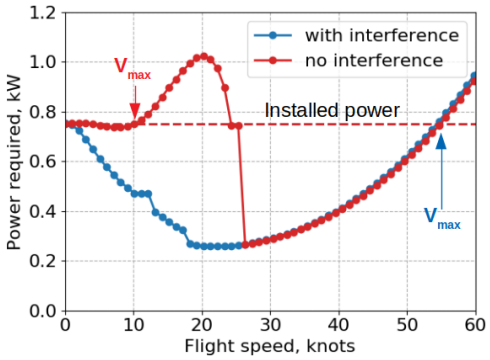

(a) Power curve

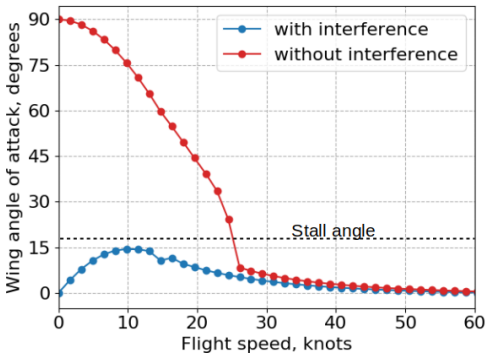

(b) Wing angle of attack

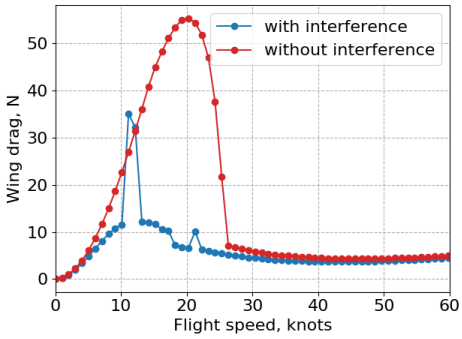

(c) Wing drag

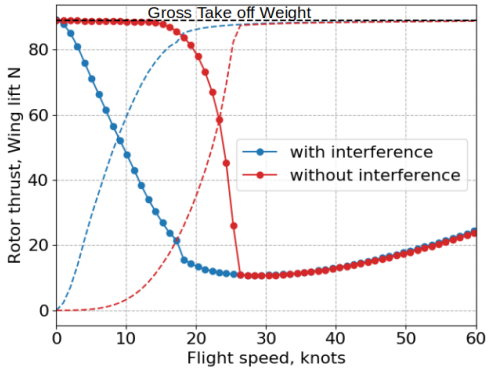

(d) Rotor thrust and wing lift

Fig. 9. Variation of vehicle thrust, lift, and power as a function of forward flight with and without the interference effect of the propwash on the wing.

forward flight speed increases and approaches cruise speed, flow over the wing attaches and there is a sharp drop in power required; the rest of the trend continues as expected. This stall delay/avoidance was also observed experimentally by Hrishikeshavan et al. (Ref. 18), and noted in numerical studies by Reddinger et al. (Ref. 19).

In transition, the angle of attack experienced by the fixed wing is shown in Fig. 9(b). In this configuration, the wing chord line is placed parallel to the vehicle body X-axis. The fuselage attitude with respect to the freestream is mathematically equal to the wing angle of attack. For low forward flight speeds, without any interference, the wing angle of attack is large and gradually decreases from 90° with increasing forward airspeed . However, with the presence of the propwash, the wing angle of attack (for sections under the propwash) is quite low and reaches a maximum of only 15°.

Figure 9(c) shows the resulting wing drag as a function of flight speed with and without the interference effect. There is an increase in wing drag (without interference), which reaches a maximum at a flight speed of 20 knots and then decreases sharply. This rise and fall is a combination of (i) the drag coefficient variation with wing angle of attack, and (ii) an increase in the dynamic pressure. All these effects are ultimately reflected in the power required to produce rotor thrusts and trim the vehicle; these comparisons are shown in Figs. 9(a) and 9(d), respectively. For the case without any interference, the rotor thrust remains high (almost at hover value) till 15 knots. However, with the presence of the propwash, the rotor thrust decreases with an increase in forward flight speed. The sharp gradients in solution in Fig. 9 for the "with interference" case is a result of static trim and the nature of the airfoil tables (stall angle of attack). For a dynamic transition maneuver with accelerations, these discontinuities may be so prominent.

Table 3 also shows that with or without interference, the sizing result remains the same; however, without including the interference effect, the motor power margins (and weight) may not be accurately captured during vehicle construction and component selection; the consequence of excluding this interference effect is that payload may be reduced after sizing because of erroneous over-sizing of the motors.

Vehicle Configurations

Figure 10 shows the four configurations that are explored as part of the study. The quad-copter and hexacopter design feature multiple edgewise rotors with RPM control for each rotor. The rationale behind these two configurations is to understand the effect the number of rotors have on the vehicle design. A quad-rotor bi-plane tailsitter (QBiT) design was also explored, where the vehicle operates in a quad-rotor mode in hover, and as a biplane in cruise. The presence of wings may reduce the power requirements in cruise and enable longer range/more endurance. The proprotors also operate predominantly in axial flight, enabling lower vibrations and better rotor performance. A lift-augmented tricopter design was also considered where the front rotor and fixed wing are tiltable as a single unit; the front rotor can act as a propeller in cruise as well as a variable-RPM rotor in hover. The rear rotors always operate in edgewise flight. The fuselage of the tricopter is not required to tilt significantly to achieve trim. In the present study, the three rotors of the tri-copter are assumed to be identical. The airframe of the configurations that carry the primary loads from the rotors and wings and house the package prior to delivery is also shown in Fig. 10.

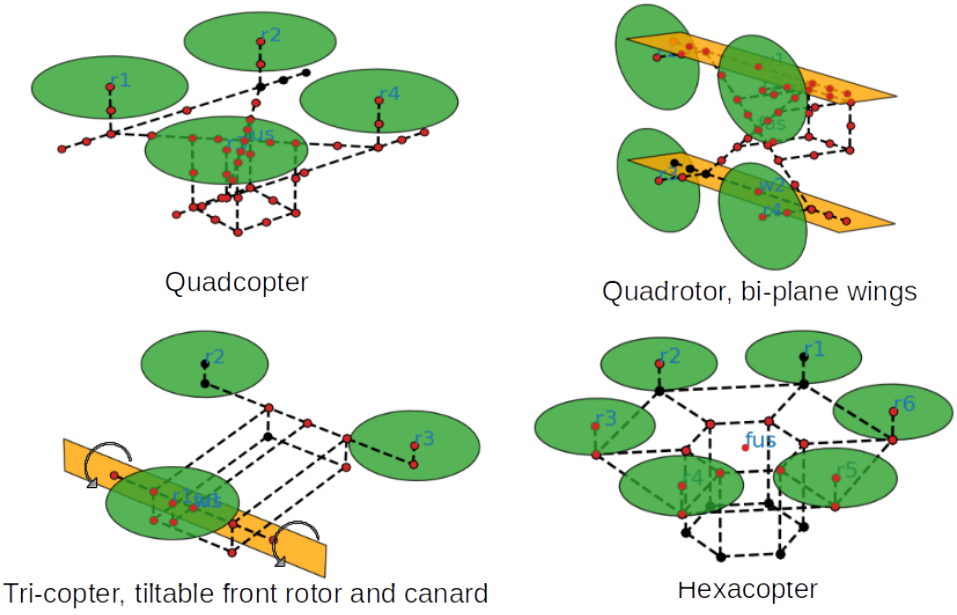

Fig. 10. Schematic of configurations along with the FEA framework of the airframe.

Mission Profile and Design Strategy

The mission profile chosen for this study emulates a simple package drop and return. These segments are shown in Fig. 11. The six mission segments are:

1. Hover for 1 minute, which approximates for lift-off followed by a minute of outbound transition with payload
2. Cruise at a steady speed, V_{cruise} for a distance d
3. One minute hover segment for inbound transition and landing at target location along with payload drop
4. Another minute-hover segment for take off and outbound transition without payload
5. Cruise back to base at V_{cruise} for a distance d without package
6. One minute hover for inbound transition and landing at base

Table 4. Design space

Configurations	Quadcopter, Hexacopter Tricopter, QBiT
Cruise speed, knots	20, 30, 40, 45, 55, 65
Range, km	5, 10, 20, 30, 40, 50
GTOW, kg	10, 15, 20, 25

The vehicle selection strategy involves identifying a vehicle that can complete the highest number of prespecified missions; the goal is to obtain a configuration that is as mission flexible as possible. The sequence of steps is as follows

1. Choose a vehicle configuration (quad, hex, QBiT or tri copter) and take-off weight (10 kg, 15 kg, 20 kg or 25 kg)
2. Sweep through a list of missions (defined by a combination of cruise speed and cruise range), listed in Table 4, for a total of 36 missions per configuration per weight category

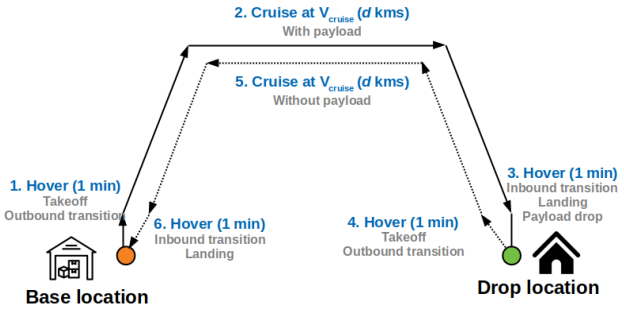

Fig. 11. Representative schematic of an idealized payload drop mission.

3. For each vehicle, perform a factorial search of the design variables: rotor radius, blade loading coefficient, hover tip-speed, ratio of RPM in hover to cruise, wing aspect ratio, and wing lift-coefficient (listed in Table 5; the last two are included only for configurations with a wing)
4. For the parametric sweep over design variables, perform sizing and identify vehicle payload that can be delivered for the given mission profile. Identify the vehicle design with maximum useful load. For different mission profiles, the payload that can be delivered by this specialized point design is unique to the design range and cruise speed.
5. For each valid design in the previous step, estimate the total energy and battery weight required to complete the other missions (parameterized by cruise speed, cruise range and payload)
6. If the total useful load (battery mass + payload mass) can be accommodated by the point design being evaluated, assign one point for that design for each off-nominal mission it can successfully complete.
7. Choose the vehicle with the maximum number of points $\rightarrow$ this is the vehicle with maximum mission flexibility

A vehicle with the maximum number of points implies it possesses the ability to serve a wide geographical area, and carry different combinations of battery and payload mass according to the mission specifications. Different cruise speeds are considered to identify the sensitivity to this parameter, because future regulations or sensor range specifications may impose effective airspeed limits.

Table 5. Design variables for factorial search

Design variable	Parametric space
Rotor radius, m	0.1, 0.2, 0.4, 0.5
Hover tip speed, m/s	100, 150, 170
Hover blade loading	0.08, 0.12
Cruise RPM ratio	0.8, 0.9, 1.0
Wing aspect ratio	8, 10
Wing lift coefficient	0.6, 0.65

Studies at Different GTOW

The four configurations were compared at 4 different take-off mass categories: 10, 15, 20 and 25 kg. Table 6 details key performance and weight parameters of the quadrotor, hexarotor, QBiT and tricopter. The payload capacity of the four configurations indicates that the quadrotor, QBiT and hexacopter have similar payload capacities across all weight classes, with the tri-copter lacking in comparison owing to a higher empty weight. The tricopter and QBiT, being winged configurations, have a much higher cruise speed of 45 knots and 65 knots, respectively, when compared to the pure edgewise configurations of quadcopter and hexacopter, which are limited to a

Table 6. Key characteristics of all configurations. Reported range, payload and battery corresponds to point design targets for maximum mission flexibility

Configuration	GTOW (kg)	Payload (kg)	empty (kg)	Battery (kg)	Range (km)	V_{CRUISE} (knots)	Delivery time (mins)
Quadcopter	10	5.97	3.29	2.03	10	20	16.2
	15	9.68	3.29	2.03	5	20	8.1
	20	13.22	44.4	2.38	5	30	5.4
	25	15.91	5.84	3.25	5	20	8.1
Hexacopter	10	6.49	2.37	1.14	5	30	5.4
	15	9.24	4.02	1.74	5	20	8.1
	20	12.05	5.22	2.73	5	20	8.1
	25	15.73	6.40	2.87	5	30	5.4
QBiT	10	6.34	2.97	0.7	5	65	2.5
	15	9.61	4.2	1.18	5	65	2.5
	20	12.89	5.42	1.69	5	65	2.5
	25	15.6	7.64	1.76	5	55	2.9
Tricopter	10	5.53	3.57	0.89	5	45	3.6
	15	7.53	6.23	1.25	5	45	3.6
	20	8.84	9.54	1.62	5	45	3.6
	25	11.55	11.33	2.11	5	45	3.6

Table 7. Design variable of all configurations at different GTOWs

Configuration	GTOW (kg)	Radius (m)	Tip-speed (m/s)	Cruise RPM Ratio	Hover C_T/σ	Wing span (m)	Wing aspect ratio	Wing C_L
Quadcopter	10	0.3	160	0.8	0.12	-	-	-
	15	0.3	160	0.8	0.12			
	20	0.3	160	0.8	0.12			
	25	0.4	160	0.8	0.12			
Hexacopter	10	0.2	160	0.8	0.12	-	-	-
	15	0.3	160	0.8	0.12			
	20	0.3	160	0.8	0.12			
	25	0.3	160	0.8	0.12			
QBiT	10	0.3	160	0.45	0.12	1.25	10	0.65
	15	0.3	160	0.45	0.12	1.29	10	0.65
	20	0.3	160	0.45	0.12	1.50	10	0.65
	25	0.4	160	0.45	0.12	1.98	10	0.65
Tricopter	10	0.3	160	0.8	0.12	1.82	6	0.65
	15	0.4	160	0.8	0.12	1.45	6	0.65
	20	0.5	160	0.8	0.12	1.67	6	0.65
	25	0.5	160	0.8	0.12	1.87	6	0.65

cruise speed of around 20–30 knots. The consequence is being able to reduce the delivery times from around 8 minutes to 2.5 minutes for a package delivered 5 km away. The power requirement for wing-borne flight are lower by 0.50–0.75 kW at 20 kg GTOW. The range and cruise speed indicate the distance and speed at which the vehicle can carry the design payload. It is possible to trade battery weight for payload, and therefore, explore payload combinations for different ranges and speed.

Table 7 shows the design variables of the "best" vehicle for each configuration at the different weight classes. Certain design variables, such as rotor blade loading coefficient, and wing lift coefficient, always gravitate towards one of the bounds of the parametric sweep. A high blade loading coefficient (C_T/σ) implies a higher lift carrying capacity of the rotor, and will result in a rotor with smaller radii or lower tip-speed. However, as a higher-order performance model (such as BEMT) is not included in this study, practical limits were imposed on the blade loading coefficient to allow for sufficient control authority for maneuvers and gust rejection, and

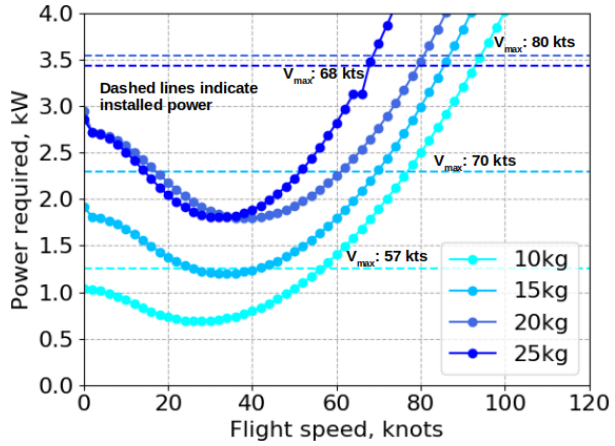

(a) Power curve

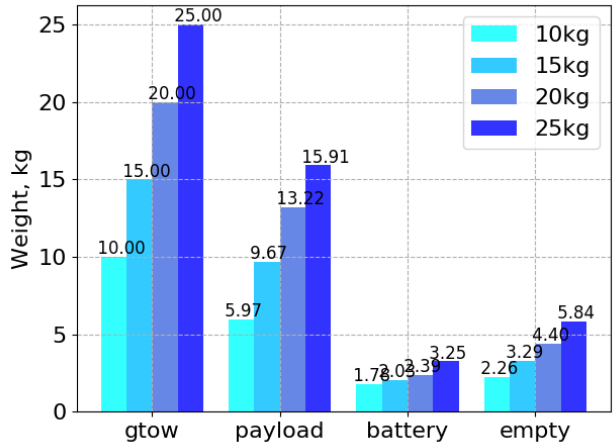

(b) Total weight breakdown

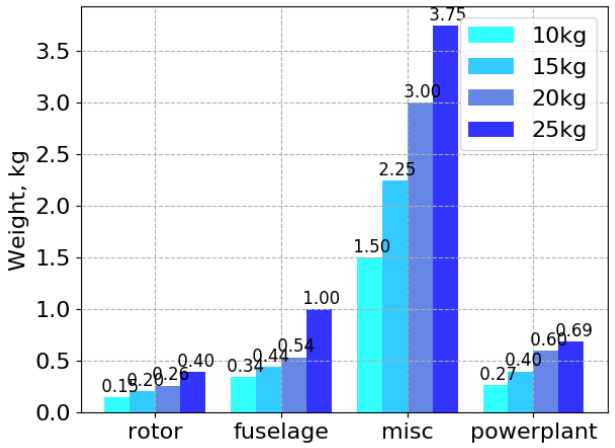

(c) Empty weight breakdown

Fig. 12. Comparison of quadcopter at multiple GTOWs.

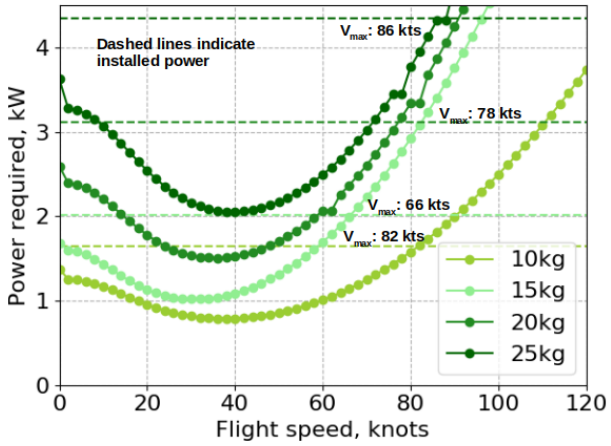

(a) Power curve

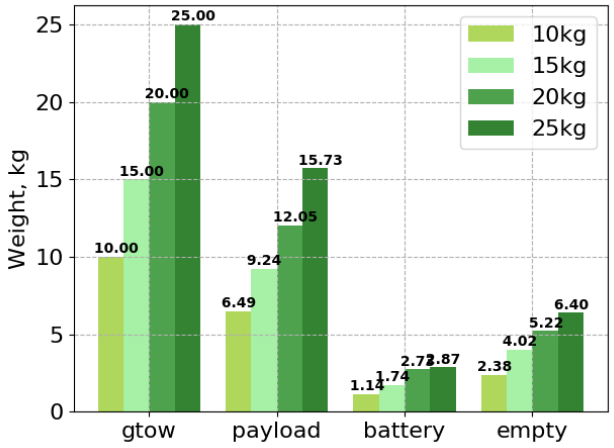

(b) Total weight breakdown

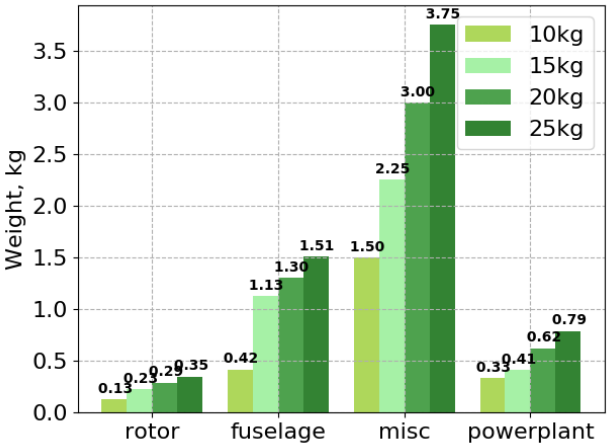

(c) Empty weight breakdown

Fig. 13. Comparison of hexacopter at multiple GTOWs.

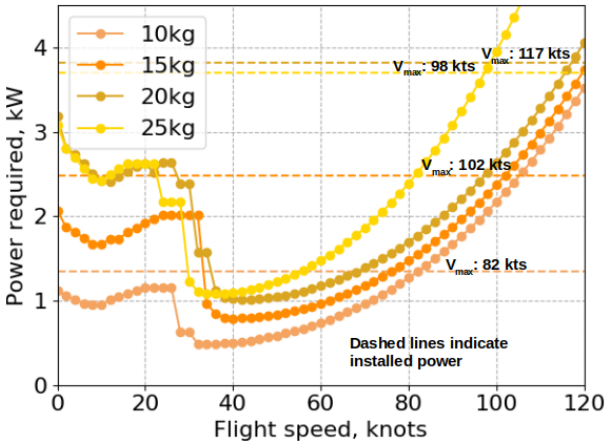

(a) Power curve

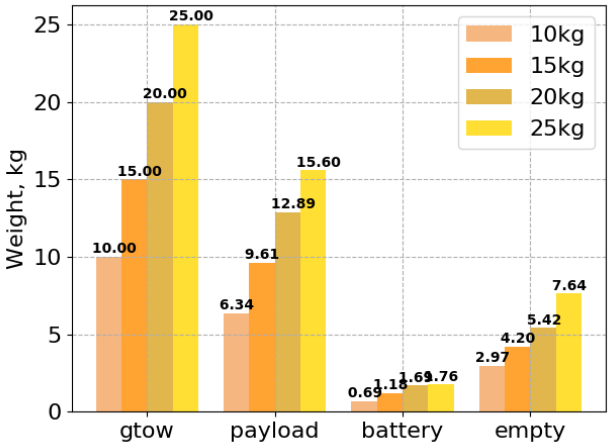

(b) Total weight breakdown

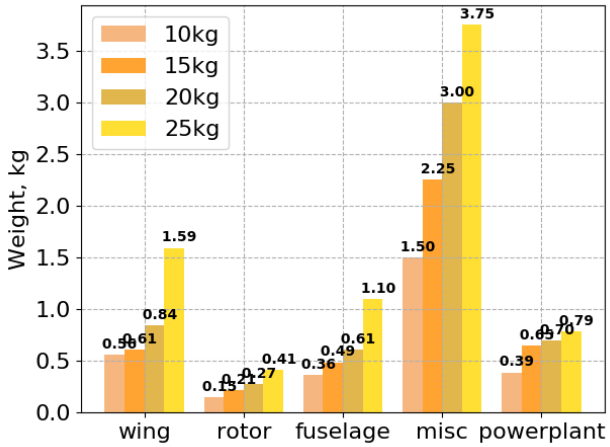

(c) Empty weight breakdown

Fig. 14. Comparison of QBiT at multiple GTOWs.

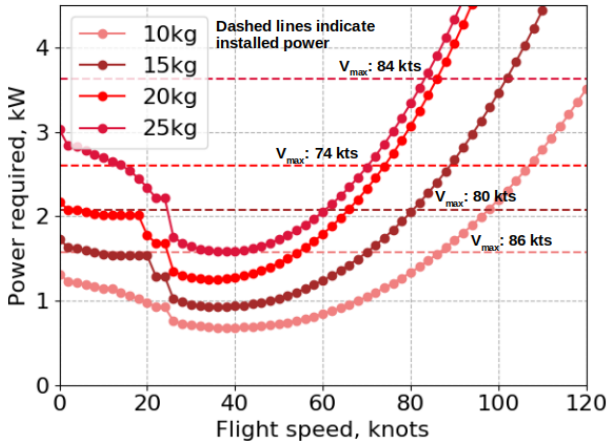

(a) Power curve

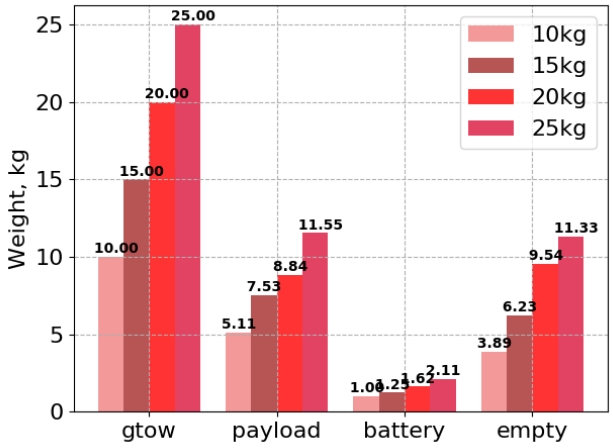

(b) Total weight breakdown

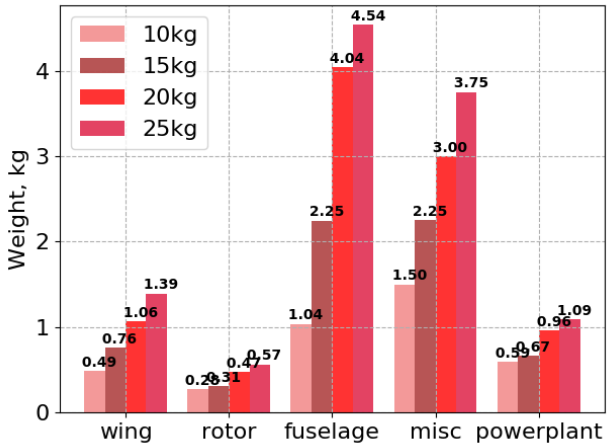

(c) Empty weight breakdown

Fig. 15. Comparison of tricopter at multiple GTOWs.

hence was capped at 0.12. Similarly, a higher wing-loading coefficient results in a wing with a lower wing-area for the same lift, and hence reduces the wing weight and therby the empty weight of the vehicle. In this study, the lift-coefficient was capped at 0.65. Cruise RPM ratio (ratio of RPM in cruise to that of hover) attempts to improve the forward flight efficiency of the vehicle. Considering most missions are biased towards cruise, to minimize the weight of the battery, a low cruise power is preffered. This result is reflected in the reduction of cruise RPM by over 55% for winged configurations; similar hover-to-cruise RPM ratios have been proposed for prop-rotors driven by electric motors (Ref. 12). The edgewise configuration also show a reduction in cruise RPM by 20% when compared to hover. Another constraint placed on the design was that of disk-loading, which was limited to 200 N/m^2. Under standard sea-level conditions, in hover, and using basic momentum theory, this disk-loading translates to downwash in the wake of 65 kmph. This constraint was imposed as the design methodology favours a smaller rotor to improve cruise efficiency, but one that has high disk loadings. Being a package delivery vehicle, a large downwash velocity would be a hindrance to customers.

Figures 12–15, each shows a set of three plots containing the power curve, total weight and empty weight breakdown for the four different weight classes for the quadcopter, hexacopter, QBiT and tricopter, respectively. Each configuration has a different base colour that is maintained through the results section. The power curve has a dashed line that indicates the installed power, which is 20% higher than the the hover power; a margin provided for transition and gust response. There are instances with certain kinks in the curve, most notably in the QBiT and tricopter designs (Figs. 14(a) and 15(a)) in the flight regime during transition from hover to cruise flight. The sharp drop in power is indicative of the airfoil sections of the wing operating at an angle of attack prior to stall, when the section drag sharply decreases; see Fig. 4(b). In a practical maneuver, a static trim would not be required, but a smooth dynamic transition would be performed. Regardless, the power curves show that sufficient power is present in the vehicle to allow for a static solution at any given flight speed during transition.

Fig. 14(a) shows that the power first decreases and then increases (around 20 knots) before decreasing sharply (around 40 knots). The earlier increase in power is a consequence of only a part of the wing being under the influence of propwash. For the 20 kg QBiT vehicle, the rotor radius is 0.3 m and the wing span is 1.50 m. The wing span under propwash is 0.85 m assuming a fully contracted wake. Therefore, part of the wing is operating a low angles of attack resulting in lower drag compared to sections that are operating at higher angles of attack. The influence of wing sections under propwash was explained earlier; see Fig. 9. Therefore, a smoother transition profile can be obtained with wings of lower span due to this beneficial interference.

Studies at GTOW 20 kg

The four vehicle configurations at 20 kg GTOW are considered in this section to perform a deep-dive into the pros and cons of specific configurations. Similar studies can be performed for the 10 kg, 15 kg, and 25 kg, but have not been presented for brevity. These designs scored the maximum number of points in being able to satisfy the most number of alternate mission profiles. Table 8 shows the vehicle parameters of the best design for each configuration along with key performance metrics, such as the maximum payload that can be delivered and the maximum operating radius.

Table 8. Characteristics of the best design for 20 kg GTOW

Parameter	Quadcopter	Hexacopter	QBiT	Tricopter
Payload delivery parameters				
Design payload, kg	13.22	12.05	12.89	8.84
Design range, km	5	5	5	5
Design speed, knots	30	20	65	45
Delivery time, min	5.4	8.1	2.5	3.6
Geometric parameters				
Rotor radius, m	0.3	0.3	0.3	0.5
Hover tip speed, m/s	160	160	160	160
Hover blade loading	0.12	0.12	0.12	0.12
Cruise RPM ratio	0.8	0.8	0.45	0.8
Wing aspect ratio	-	-	10	6
Wing lift coefficient	-	-	0.65	0.65
Performance parameters				
Installed power, kW	3.54	3.11	3.82	2.60
Speed: best endurance, knots	38	36	43	34
Speed: best range, knots	60	58	70	56
Maximum speed, knots	81	78	117	72
Cruise lift-to-drag	2.11	1.51	9.13	4.44

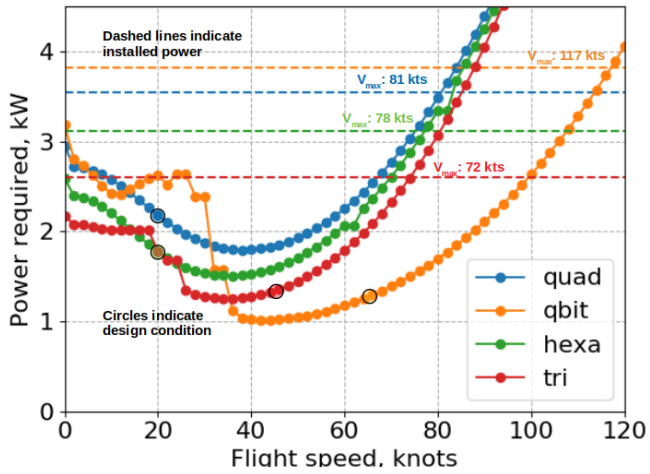

(a) Power curve

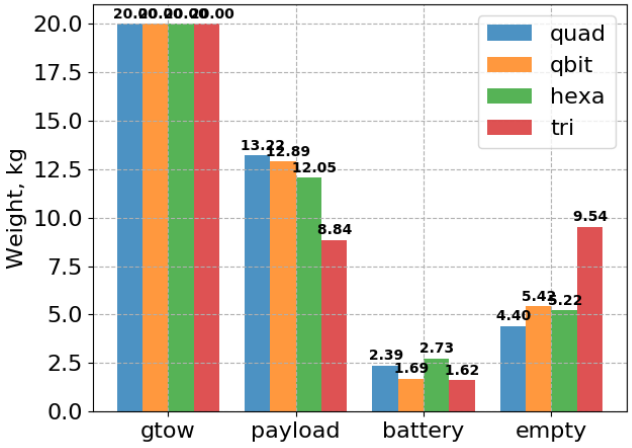

(b) Total weight breakdown

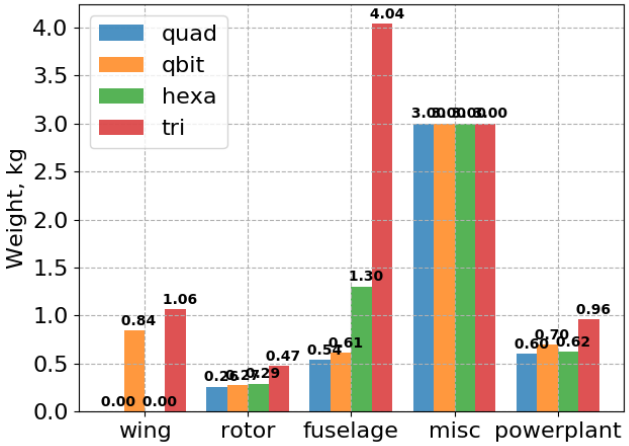

(c) Empty weight breakdown

Fig. 16. Comparison of configurations at GTOW of 20 kg. Dashed lines indicate installed power.

Table 8 also shows key performance parameters across the configurations. Amongst the configurations, the tricopter requires the least installed power because of the highest rotor radius which results in the lowest disk loading. The tricopter is a compromised design, as in this study, dissimilar rotors were not considered for the fore and aft rotors. Therefore, the same rotor design is expected to perform edgewise (rear rotors) as well as the prop-rotor functionality of the forward rotor. This configurations limits the maximum forward flight of the vehicle to 72 knots compared to the QBiT whose rotors operate only in axial flight condition, and results in a maximum forward flight speed of 117 knots. Additionally, the flat plate area of the tricopter is higher than that of the QBiT. The power curve of the different configurations at 20 kg GTOW are shown in Fig. 16(a).

Figures 17(a) and 17(b) shows the wing tilt orientation along with the thrust generated by the three rotors along with the wing lift at various flight speeds for a 20 kg tricopter. The initial orientation of the wing is 90°, and then reduced to 0°, indicating airplane mode, as shown in Fig. 17(a). The fuselage does not tilt and therefore, the aft rotors are constantly operating in edgewise flow. To maintain longitudinal moment balance, the aft rotors produce a net thrust that is equal to half the weight of the vehicle irrespective of the flight condition, as shown in Fig. 17(b). Therefore, these rotors are effectively operating at a point design for blade-loading coefficient (C_T/σ). Unlike traditional helicopter rotors, the individual rotors need not be trimmed to zero rolling moment or pitching moment; the relaxation of this strict requirement allows for extracting more lift from the edgewise rotors in forward flight.

The forward rotor and the wing effectively trade the thrust and lift produced, respectively, as the flight speed increases. This requirement of high loads on the airframe in all flight condition may be responsible for the high airframe weight (Fig. 16(c)). In follow-on studies, this configuration could be explored for various combinations and rotor and wing placement and lift/thrust share, that may yield a design with higher useful load.

Between the two edgewise configurations, the hexarotor has a lower installed power compared to the quadrotor owing to a lower disk loading. Both configurations have the same rotor radius and tip-speed. The hexarotor suffers a minor penalty in the payload it can carry (12.05 kg), when compared to the quadrotor which is designed to carry 13.22 kg. While the hexarotor has a higher fuselage weight compared to the quadrotor, the lower power requirements result in a lower battery weight and a higher payload weight; see Figure 16(c) and Table 6.

Figures 18(a), 18(b), 18(c) and 18(d) show a contour map of payload for different combinations of radius of action and cruise speed for each of the configurations. For each combination of range and cruise speed, the payload that can be carried by the "best" design of each configuration is evaluated. Based on the distance of the delivery location from the target, the maximum deliverable payload can be estimated along with the cruise speed (or indirectly, the time of delivery) can be cal-

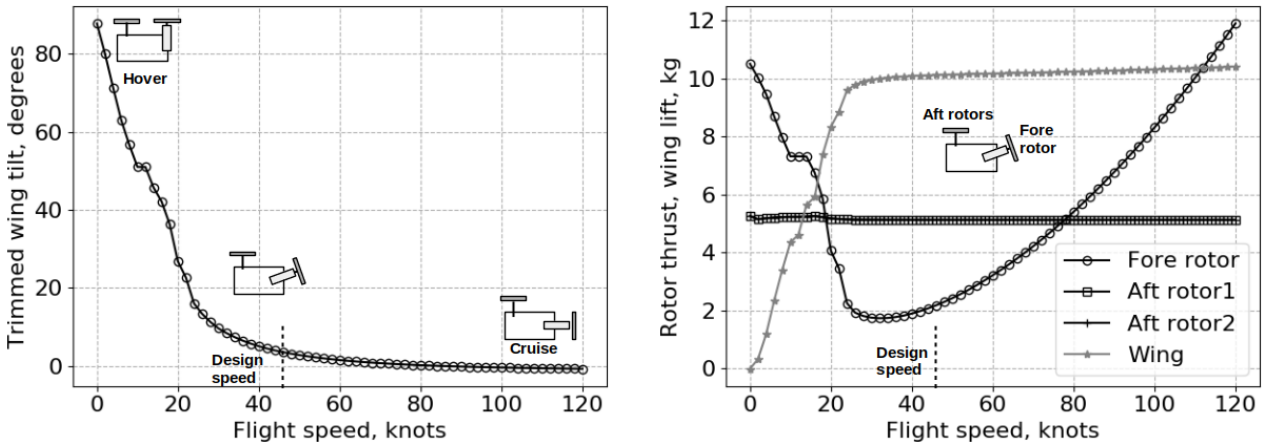

(a) Wing tilt

(b) Thrust and lift

Fig. 17. Wing tilt, thrust and lift generation for the 20 kg tricopter at various forward flight speeds.

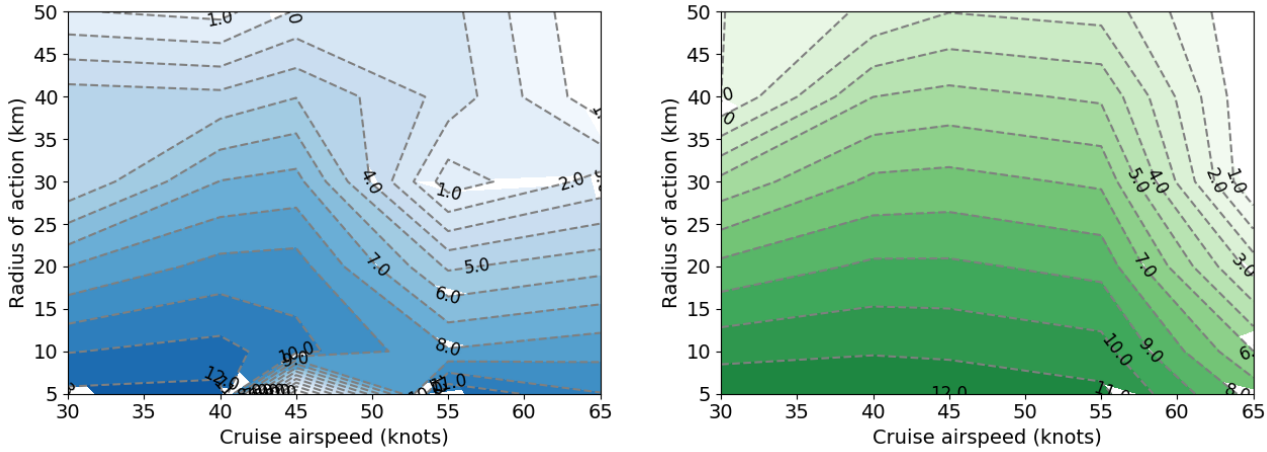

(a) Quadcopter

(b) Hexacopter

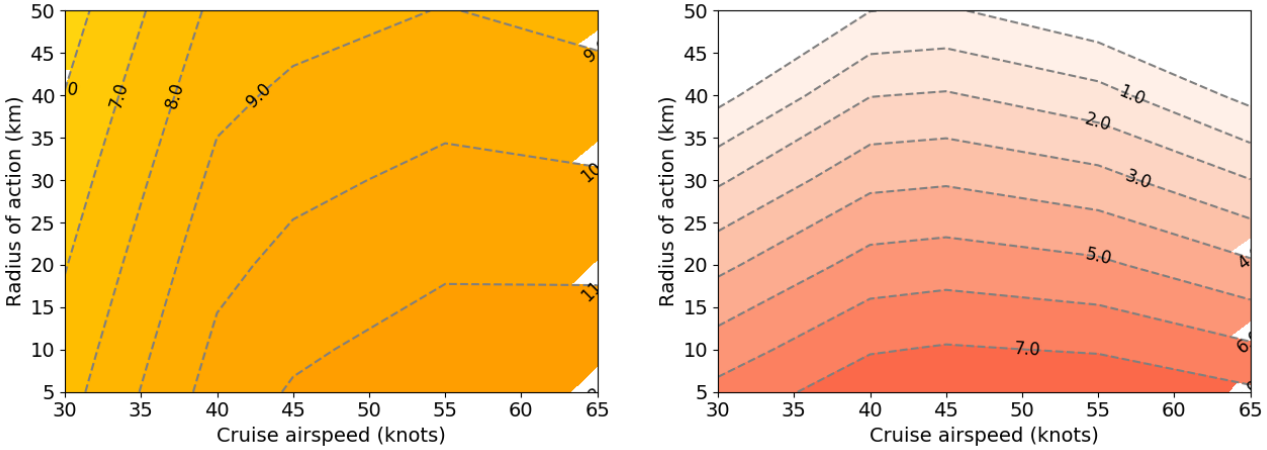

(c) QBiT

(d) Tricopter

Fig. 18. Contour maps of payload for multiple combinations of range and cruise speed at 20 kg for all four configurations.

culated. As an example, tracing the iso-contour line of 5 kg payload in Fig. 18(a), the 20 kg quadcopter can deliver the payload 35 kms away at a cruise speed of 45 knots or deliver at 60 knots to a distance of around 20 kms. These isocontour lines are a direct consequence of the power requirements of the vehicle in forward flight. The useful load, i.e., the battery weight and payload, can be traded to either deliver a larger payload nearby or a smaller payload at a location that is further away.

The QBiT, as shown in Fig. 18(c), has a radius of action wherein a larger payload weight can be delivered when compared to the other configurations. Packages as heavy as 11 kg can be delivered as far as 15 kms away at a high cruise speed of 65 knots, owing to the lower power requirements of the QBiT in forward flight, therby establishing the need for a lift-augmented vehicle for these mission. The tricopter (Fig. 18(d)) while lift-augmented does not feature the same levels of performance as the QBiT owing to the rotors that constantly operate in edgewise flow. Owing to the lower installed power of the tricopter, the total battery weight that can be traded into payload weight is also lower, which renders it unable to carry payloads greater than 7.5 kg.

SUMMARY AND CONCLUSIONS

Four vehicle configurations, i.e., quadrotor, hexarotor, quadrotor bi-plane tailsitter (QBiT) and a lift-augmented tricopter were studied in their ability to perform a representative package delivery mission at weight classes ranging from 10 kg – 25 kg. The "best" vehicles were obtained through a conceptual sizing methodology (HYDRA) based on their ability to perform a wide range of missions, to maximize the mission flexibility of the vehicle. Care was taken to include allowances in the design for flight maneuvers and tolerance to gust, while also imposing certain constraints such as the disk loading on rotors to minimize the downwash beneath the vehicle during payload delivery. A battery powered all-electric vehicle was the powerplant considered for all configuraitons. Key conclusions from this study are as follows,

1. The presence of the propeller ahead of the wing performs a dual role of increasing the dynamic pressure on the wing and reducing the sectional angle of attack, thereby allowing for a smooth flight transition from hover to cruise. In the absence of propwash, the power requirements during transition can increase by as much as 20% and can limit the performance of the vehicle. Consequently, a propeller wing combination benefits from a tractor design as opposed to a pusher design.

2. A consequence of the above inference is that for configurations with propeller-wing combination, a design where the entire span is under the wash is preferred to one where part of the wing is under the propwash. The sections of the wing that are not influenced by the propeller wake produce high drag, which causes an increase in shaft power during transition. Therefore, multiple smaller rotors might be preferred to one larger rotor over a wing subject to other factors such as disk loading and/or forward flight efficiency.

3. Between the two edgewise configurations considered (quadcopter and hexacopter), the hexacopter was able to deliver heavier packages at further distances compared to the quadcopter. Both vehicle have a cruise speed that lies in 20 knots – 30 knots range, but the hexacopter requires lower power owing to six rotors each operating at a lower disk loading compared to the quadcopter for the same GTOW. The forward flight speed is limited by the relatively high flat-plate area compared to the other "tiltable" configurations of QBiT and tricopter.

4. The lift-augmented tricopter features a propeller mounted on a tilting fixed wing in the front and two edgewise rotors in the back. The tricopter has a lower power requirement in cruise and higher cruise speed compared to the edgewise configurations, but is more mechanically complex than the quad-rotor or hexacopter. The tri-copter represents a marginal increase in flight control system complexity for a large increase in cruise speed. Allowing for dissimlar rotors should allow for improved designs of this configuration.

5. Among the configurations investigated, the QBiT is the most effective in terms of payload delivery and radius of action; it is also mechanically as simple as the hexacopter or quad-rotor designs. However, the complexity in this configuration lies in the flight control system, where more investment in terms of flight software design may be required. Transition from hover to cruise involves understanding and quantifying complex aerodynamic interactions between the rotor and wing. With iterative development and refinement, it may be possible to achieve reduced package delivery time at higher forward flight speeds with this platform.

REFERENCES

[1]"First FAA sanctioned use of a drone for routine revenue flights involving the transport of a product under a contractual delivery agreement, accessed July 20, 2019," https://pressroom.ups.com/pressroom/, Mar 2019.

[2]"Zipline, which delivers lifesaving medical supplies by drone, now valued at $1.2 billion, accessed July 20, 2019," https://www.cnbc.com/2019/05/17/zipline-medical-delivery-drone-start-up-now-valued-at-1point2-billion.html, May 2019.

[3]"Melbourne start-up Swoop Aero wins first contract to deliver vaccines via drones, accessed July 20, 2019," https://www.afr.com/technology/melbourne-startup-swoop-aero-wins-first-contract-to-deliver-vaccines-via-drones-20181023-h16z7m.

[4]"Rhaegal RG-1, accessed July 20, 2019," https://www.sabrewingaircraft.com/cargo-uav/, July 2019.

[5]"A Startup's Plan To Cut Air Freight Costs In Half With 777-Size Drones, accessed July 20, 2019," https://www.fastcompany.com/3069053/a-startups-plan-to-halve-cargo-shipping-costs-with-777-size-drones, Mar 2017.

[6]Sidle, S., Bogdanowicz, C., Gudenius, B., Shishika, D., Wang, X., Winslow, W., Nagaraj, V. T., and Chopra, I., "AirEZ: 32nd Annual Student Design Competition," Technical report, University of Maryland, College Park, 2014.

[7]Sridharan, A., Govindarajan, B., and Chopra, I., "A Scalability Study of the Multirotor Biplane Tailsitter using Conceptual Sizing," *Journal of the American Helicopter Society*, 2019.

[8]Sridharan, A., Govindarajan, B., Nagaraj, V. T., and Chopra, I., "Design Considerations of a Lift-Offset Single Main Rotor Compound Helicopter," American Helicopter Society Aeromechanics Design for Vertical Lift, San Francisco, CA, January 20–22, 2016.

[9]Govindarajan, B., Sridharan, A., and Chopra, I., "A Scalability Study of the Multirotor Biplane Tailsitter using Conceptual Sizing," Proceedings of the 74th Annual Forum of the American Helicopter Society, Phoenix, AZ, May 14–17, 2018.

[10]Govindarajan, B., Sridharan, A., and Avera, M., "Integration of Physics Based Weight Models into Rotorcraft Design Sizing," 43rd European Rotorcraft Forum, Milan, Italy, September 12–15, 2017.

[11]De Marco, A., Duke, E., and Berndt, J., "A general solution to the aircraft trim problem," AIAA Modeling and Simulation Technologies Conference and Exhibit, 2007.

[12]Droandi, G., Syal, M., and Bower, G., "Tiltwing Multi-Rotor Aerodynamic Modeling in Hover, Transition and Cruise Flight Conditions," Proceedings of the 74th Annual Forum of the American Helicopter Society, Phoenix, AZ, May 14–17, 2018.

[13]Jones, E., Oliphant, T., Peterson, P., *et al.*, "SciPy: Open source scientific tools for Python, accessed Mar 20, 2019," https://www.fastcompany.com/3069053/a-startups-plan-to-halve-cargo-shipping-costs-with-777-size-drones, 2001–.

[14]Phillips, P., Hrishikeshavan, V., Rand, O., and Chopra, I., "Design and Development of a Scaled Quadrotor Biplane with Variable Pitch Proprotors for Rapid Payload Delivery," Proceedings of the 72nd Annual Forum of the American Helicopter Society, West Palm Beach, FL, May 17–19, 2016.

[15]Winslow, B. M. H. J., J. and Chopra, I. C., "Design, Development, and Flight Testing of a High Endurance Micro Quadrotor Helicopter," *Journal of Micro Air Vehicles*, Vol. 8, (3), 2016, pp. 155–169.

[16]Hoerner, S. F, *Fluid Dynamic Drag*, Self Published, 1965.

[17]Johnson, W., "NDARC - NASA Design and Analysis of Rotorcraft Validation and Demonstration," American Helicopter Society Aeromechanics Specialists Meeting, San Francisco, CA, January 2008.

[18]Hrishikeshavan, V., Bogdanowicz, C., and Chopra, I., "Design, Performance and Testing of a Quad Rotor Biplane Micro Air Vehicle for Multi Role Missions," *Journal of Micro Air Vehicles*, 6 2014, pp. 155–173.

[19]Reddinger, J. P., McIntosh, K., Zhao, D., and Mishra, S., "Modeling and Trajectory Control of a Transitioning Quadrotor Biplane Tailsitter," Vertical Flight Society 75th Annual Forum, Philadelphia, PA, May 13–16, 2019.